Matter

CellPress
OPEN ACCESS

Article

In operando 3D mapping of elastic deformation fields in crystalline solids

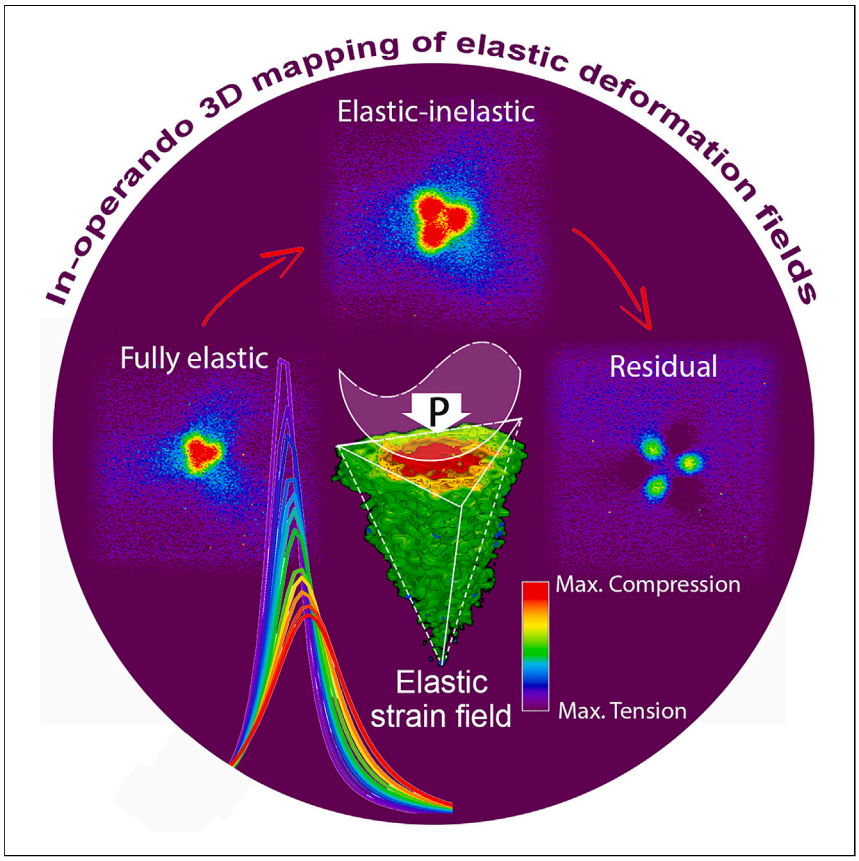

Understanding elastic deformation fields (EDFs) in anisotropic and heterogenous materials requires complex approaches that allow measurements under applied stresses, *in operando*, in 3D, and with a high spatial resolution. So, their measurements remain challenging. We introduce a desktop methodology by which the formation and development of complex EDFs in Raman-active materials can be simultaneously mapped under varying applied loads, in 3D, and with submicron resolution. Our method opens a new avenue for investigating the mechanical deformations in complex materials and microdevices.

Shahrouz Amini, Tingting Zhu, Hajar Razi, Erika Griesshaber, Peter Werner, Peter Fratzl

shahrouz.amini@mpikg.mpg.de (S.A.)
peter.fratzl@mpikg.mpg.de (P.F.)

Highlights

In operando mapping of elastic deformation fields (EDFs) under varying applied loads

Unraveling the evolution of elastic and inelastic deformations in complex materials

Direct visualization of EDFs without assumptions such as roughness and Poisson's ratio

Simultaneous 3D mapping of EDFs and microarchitecture, including organic components

Development
Practical, real world, technological considerations and constraints

Amini et al., Matter 7, 2591–2608
July 3, 2024
https://doi.org/10.1016/j.matt.2024.06.006

Matter

CellPress
OPEN ACCESS

Article

In operando 3D mapping of elastic deformation fields in crystalline solids

Shahrouz Amini,[1,4,*] Tingting Zhu,[1] Hajar Razi,[2] Erika Griesshaber,[3] Peter Werner,[1] and Peter Fratzl[1,*]

SUMMARY

Revealing the distribution of elastic deformations in anisotropic solids is of crucial importance for evaluating the mechanical performance of complex materials. However, elastic deformation fields (EDFs) need to be investigated under applied loads and in 3D, so they are often limited to planar approaches or simplifying assumptions. Here, we introduce 3D-RISM, a method by which the 3D spatial distribution of EDFs can be mapped *in operando* and with submicron resolution in laser-translucent materials. Taking examples of geological and biological ceramics, we visualize the 3D distribution and stepwise development of anisotropic EDFs under Hertzian contacts. We leverage our method to showcase how the anisotropy of elastic behavior regulates the distribution of induced plasticity and the direction of microcracking in crystals. 3D-RISM offers a promising platform for real-time mapping of deformation tensors in complex materials and devices, opening new avenues for better understanding the behavior of materials with azimuthal anisotropy in Poisson's ratio.

INTRODUCTION

The quantitative understanding of the mechanical behavior of materials—the physical state of matter in response to applied stresses—requires analytical approaches by which material deformations can be analyzed under load and at different deformation stages. The evolution of mechanical deformations starts with the development of elastic (temporary) deformations. Once the applied stress exceeds a certain level, the material experiences inelastic (permanent) deformations in the form of quasi-plasticity, plasticity, or brittle cracks.[1–3] While the inelastic deformations can be studied and explained by their permanent footprints (e.g., rupture and fracture, microcracks, twinning, and dislocations), elastic deformations need to be investigated under applied stresses, *in operando*, and with a high spatial resolution. So, the measurements of elastic deformations under contact stresses remain challenging and have been largely restricted to high-resolution X-ray diffraction microscopy[4,5] in advanced synchrotron facilities or 2D approaches such as transmitted electron diffraction methods[6,7] and photoelasticity methods.[8]

Raman spectroscopy, which relies upon the inelastic scattering of photons, provides a powerful and non-destructive route to determining elastic deformations in Raman active solids,[9–14] so structural information and material deformation can be captured simultaneously. In this method, elastic deformations and the corresponding changes in chemical bond lengths can be accurately determined through changes in the vibration frequency of the molecules, which can be recorded by the peak shifts in

PROGRESS AND POTENTIAL

Despite the advances in the mechanical characterization of materials, 3D and *in operando* imaging of elastic deformation fields (EDFs) remains challenging, preventing a full assessment of complex material deformation mechanisms. This has been mainly attributed to the limitations and complexities in methodological approaches capable of simultaneously inducing, measuring, and visualizing localized EDFs with suitable spatial resolution. To address the current limitations, we devised 3D-RISM, a desktop methodology that allows the mapping of localized deformations beneath the contact loads that induce them, with submicron spatial resolution and in 3D. We anticipate that 3D-RISM can pave the way toward a quantitative understanding of the evolution of elastic deformations in complex materials and open new avenues for unraveling the interplay between elastic anisotropy, materials' microarchitecture, and mechanical performance in hybrid materials and microdevices.

associated bands in Raman spectra.[9] This technique, which requires minimal sample preparation and is often accessible in materials characterization labs, has been widely used to investigate residual strains (i.e., permanent inelastic strains) in the absence of external forces[2] and in 3D.[15] However, due to complexities in inducing, preserving, and opening optical visibility for 3D scanning of induced strain fields under a Raman microscope, the usage of this technique for probing elastic deformations (in the presence of external loads) has been mainly limited to point[15] or 2D measurements[16,17] and off-axis methods[18] inducing tip-shadowing effects. Hence, 3D mapping of elastic deformations and their evolution (elastic-inelastic transitions) remains challenging.

Here, we present a method[19] based on confocal Raman microspectroscopy combined with a designed miniaturized inverted nanoindenter equipped with a translational optical stage that together allows the mapping of induced localized deformations beneath the indenter (contact zone), *in operando*, with submicron spatial resolution, and in 3D. By relying on commercially available Raman microscopes and devising a spring-free nanoindenter, our design provides major improvements in elastic deformation visibility, load/displacement stability in long-term 3D scans, and lateral sample positioning (see system design) over previous Raman-based methods.[17,20–22] In the following sections, we delineate the method, which we termed "3D-RISM," and showcase its application to study the evolution of elastic deformation fields (EDFs) in biological and geological crystals. By taking advantage of the *in operando* capability, we demonstrate how azimuthal anisotropy of elastic behavior can influence the evolution of deformations and dictate the formation of inelastic deformations in calcite and its biological counterpart, single crystal-like prisms of *Pinna nobilis*.[23] Our approach reveals an uncommon spatial relationship between the crystallographic organization of biological calcite with externally induced strain fields, providing new insights into the underestimated role of azimuthal anisotropy in the elastic behavior of materials.

RESULTS AND DISCUSSION

System design

The layout of our system is shown in Figure 1. To establish the method, we designed and fabricated a miniaturized inverted nanoindenter using a linear piezo actuator equipped with a lockable 2D translational stage containing a large optical window. Together, the setup provides a combination of (1) accuracy in the formation of elastic deformations, (2) visibility to developed EDFs beneath the contact point, (3) stability in maintaining the applied strains during long-term volumetric mappings, and (4) simplicity in design for combining the setup with a commercial confocal Raman microscope for 3D mapping of EDFs with high spatial resolution. We achieved these criteria by designing the following series of elements. The nanoindenter, based on a high-precision linear piezo actuator and encoder, allows the application of stable positioning with nanometer resolution. The actuator is combined with a miniature load cell with 0.1-mN load resolution and a cono-spherical diamond indenter, allowing the recording of the minute applied forces and formation of localized elastic deformations, respectively. Note that using sharp indenters such as Berkovich and cube corner tips intensively localizes the contact stresses and advances the formation of inelastic deformations at the geometries below the detection limits of confocal Raman microscopy (see Figure S1 for further details). This prevents the detection and imaging of EDFs at their formation stages, so sharp tips are impractical for studying elastic stain fields using methods incapable of resolving spatial resolutions below 100 nm, such as light microscopy.

[1]Department of Biomaterials, Max Planck Institute of Colloids and Interfaces, 14476 Potsdam, Germany

[2]Wood Materials Science, Institute for Building Materials, ETH Zürich, 8093 Zürich, Switzerland

[3]Department of Earth and Environmental Sciences, Ludwig-Maximilians Universität, 80333 Munich, Germany

[4]Lead contact

*Correspondence: shahrouz.amini@mpikg.mpg.de (S.A.), peter.fratzl@mpikg.mpg.de (P.F.)

https://doi.org/10.1016/j.matt.2024.06.006

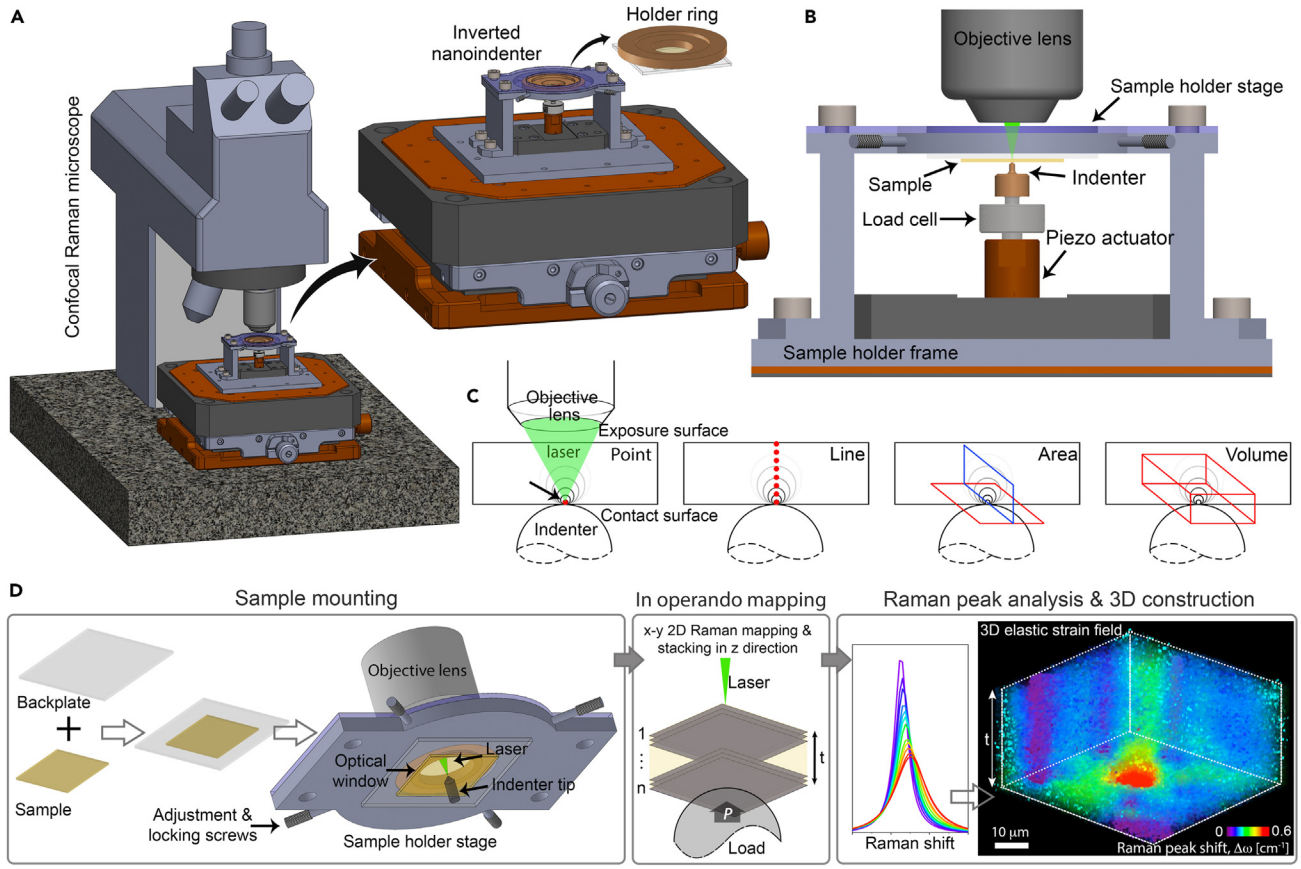

Figure 1. Design of the devised setup for *in operando* 3D elastic deformation imaging (3D-RISM)

(A) Schematic 3D model of the combined miniaturized inverted nanoindenter and confocal Raman microscope. The translational stage, composed of a positioning holder ring and locking screws sandwiched within a metallic frame, allows fine lateral positioning and mechanical stability during long-term mapping. The wide optical window integrated into the positioning ring allows the user to select and probe a series of ROIs after mounting the sample rather than changing samples between the measurements. A wide optical window provides shadow-free optical accessibility to the areas beneath the contact point and allows high-resolution mapping using high-magnification objective lenses.

(B) Side view of the setup, illustrating the arrangement of the inverted nanoindenter, stage, sample, and objective lens.

(C) Shadow-free access of the laser beam across the sample provides an apt configuration for scanning the developed EDFs beneath the contact zone in different mapping modes (point, line, area, or volume) with submicron spatial resolution.

(D) Schematic of the workflow when using 3D-RISM for the mapping of elastic deformation in translucent Raman active solids.

The stage used for mounting the samples provides shadow-free optical accessibility through a window with a large opening (d = 11 mm) required for Raman mapping of large areas (Figures 1A–1C). Moreover, the large window allows lateral positioning for selecting and probing different locations/samples rather than replacing the samples with new ones. The setup provides a minimum working distance of 3 mm, required for high-resolution Raman mapping, so high-magnification objective lenses can map the contact area without interference or with shadowing from the mechanical probe or frame elements (Figures 1A–1C). While the lateral and vertical movements required for locating the indenter are provided by the motorized stage of the Raman microscope, our designed lockable 2D translational stage (Figure 1A) allows fine sample positioning for selecting different regions of interest (ROIs). So, one can conduct indents at different locations without replacing the sample between individual indents. Finally, the stage can be locked to avoid any stage/sample movement during the measurements.

Since the probing and loading axes are parallel and co-localized, the deformation volume beneath the contact point is accessible to the laser and can be mapped in 3D. Hence, the probing zone can be in the form of a point, line, plane, or volume (Figure 1C), which can be reconstructed by stacking a series of 2D scans toward the contact point. The sample is placed on the indenter side of the translation stage, and it can be attached to the positioning ring (Figure 1A) by a supportive, laser-transparent backplate, such as a quartz slide. Finally, due to the simplicity in design, we combined the miniaturized inverted nanoindenter with a confocal Raman microscope with a high spectral resolution of 0.2–0.4 cm^{-1} (grating 2,400 gr/mm (grooves per millimeter) and 1,800 gr/mm for λ = 532 nm and 785 nm, respectively), so induced peak shifts can be accurately measured, fitted, and analyzed.

3D microscopy of EDFs in geological and biological ceramics

We leverage our devised method to experimentally unravel the evolution and development of elastic deformations in two groups of homogeneous (single crystals) and complex architectured ceramics (seashells) with intercrystalline organic envelopes and intracrystalline organic residues,[24–26] described in the following sections.

We first applied our method to investigate the development of elastic deformations in geological single crystals: a geological fluorapatite (FAP) and a geological calcite, each representing a homogeneous quantum medium yet providing different crystal symmetries; i.e., hexagonal (point group of 6/m) and trigonal (point group $\bar{3}$ 2/m), respectively. So, to understand the effect of crystal symmetry on the geometry of EDFs, the crystal models were indented along their hexagonal and trigonal symmetry axes. Accordingly, the crystals were sectioned and polished perpendicular to their *c* axis (experimental procedures) and then evaluated by X-ray diffraction (Figure S2) and polarized Raman spectroscopy[27] methods. In the case of calcite, a cutting perpendicular to the c axis (optical axis) was essential to cancel the double refringence of the crystal.[28] The crystal's transparency allowed us to use relatively thick sections (up to 0.5 mm) supported with a quartz backplate (thickness, t = 1 mm) to prevent any possible bending under localized contact loads.

To ensure the performance of measurements under elastic deformation, the threshold of the inelastic regime in each sample was defined by means of depth-sensing partial loading-unloading experiments[2] using a cono-spherical indenter to isotropically apply indentation strain fields.[29] This isotropy in applied deformation is important to visualize the possible azimuthal anisotropies in the mechanical response of the samples. A diamond indenter with a relatively large tip radius (r = 125 μm) was selected to postpone the elastic-inelastic transitions, providing a broad loading range in which EDFs can be induced, maintained, and imaged. The load resulting in the permanent residual impression was recorded as an elastic-inelastic "transition" load (P_t). Note that the term "yielding" is intentionally avoided here, since the crystals can form microcracks, and not all induced deformations form under plastic regimes.

In Raman measurements, a proper signal-to-noise ratio can be achieved by raising the laser intensity and increasing acquisition time. However, these increments can impose thermal effects and time limits in the case of high-resolution 3D Raman mapping. So, 3D Raman mapping should be performed using moderate laser intensities (depending on the sample characteristics), and selected spectral acquisition times should often stay below 1s. Accordingly, we selected the most intense peaks (963 cm^{-1} and 1,086 cm^{-1} attributed to PO_4^{3-} and CO_3^{2-} groups in FAP and calcite,

respectively) corresponding to the symmetric stretching mode (ν_1) for 3D Raman mapping and analyzing the induced peak shifts. This allowed us to decrease the spectral acquisition time to <1 s and use a laser power of ≤40 mW for our EDF mappings.

Azimuthal isotropy of EDFs in FAP

Depth-sensing partial loading-unloading nanoindentation showed a P_t of 2.8 ± 0.2 N (Figure 2A), so the load below this value was considered for the EDF studies. We started our measurements by piezo-spectroscopy calibration[30,31] and deployed a displacement control nanoindentation to correlate the applied loads and associated contact depths to shifts in the ν_1 vibrational band of the FAP (Figures 2B and 2C). Note that variations in elemental composition, such as the presence of F and Mg in calcium phosphate and calcium carbonate crystal lattice, can influence the Raman peak position.[32] Hence, to separate the effect of chemical variations and extract the mechanically induced Raman peak shift, the indentation-induced peak shifts in this work are reported as relative peak shifts ($\Delta\omega = \omega_{Deformed} - \omega_{Relaxed}$), which only include the relative peak shifts under *in operando* loading of the sample. We used Lorentzian peak fitting to extract the peak position shifts (experimental procedures), revealing a clear transition of the 3.79 Raman peak shift (cm^{-1}) under an applied load of 1.66 N (Figure 2C). Figure 2D shows the peak shift and broadening of the ν_1 band for the range of applied deformations. The peak broadening effect denotes that the phosphate bands within the sampling volume were not uniformly deformed, and the induced deformation formed a gradient within the sampling volume.

The 3D mapping experiment started by locating the diamond tip position, apparent by, first, intensive light reflection by the diamond tip prior to tip-sample contact and, later, the formation of Newton's rings while engaging the tip to the sample surface (Figure S3). Areas free from superficial defects and optically visible crystalline flaws were selected for indentation. A set load of 1 mN was defined for approaching and detecting the sample surface. Then, an applied load of 1 N (contact depth, h = 840 nm), ensuring an elastic deformation in the sample (Figure 2A), was selected to induce an EDF in the FAP sample. A volume of 80 × 80 × 40 μm^3 using a spatial resolution of 1 μm (x-y-z) was selected for the mapping of the induced elastic deformation using a 20× objective lens (numerical aperture [NA] = 0.35) and an acquisition time of 0.6 s. The 3D map was acquired by collecting a series of 2D scans (80 × 80 μm^2) from unstrained areas toward the contact surface through a stacking mode. The collected maps were processed to remove cosmic rays and spectral backgrounds, and the peaks were fitted using the Lorentzian function (experimental procedures). The extracted peak positions (X_0) were used for plotting the induced peak shift maps. Clearly, due to the differences in induced applied deformations in different scanning depths, the peak position ranges vary between the 2D scans. Therefore, for normalizing the induced peak shifts in the entire 3D map, we defined the range of the assigned color codes by selecting the minimum and maximum peak shift values within the entire individual 2D scans. Finally, the 2D maps normalized for the peak shift range were reconstructed into a 3D map using ImageJ Volume Viewer and Amira (Figure 2E). The reconstructed 3D peak shift map of the induced deformation and corresponding calculated indentation stress and strain fields[2] revealed a continuum contact EDF representing a Hertzian strain field in brittle solids.[29] The associated applied contact stress and strains calculated using Hertz's model[2,33] revealed that the induced EDF was developed under a maximum contact stress of 1.54 GPa and indentation strain of 11.5%, respectively.

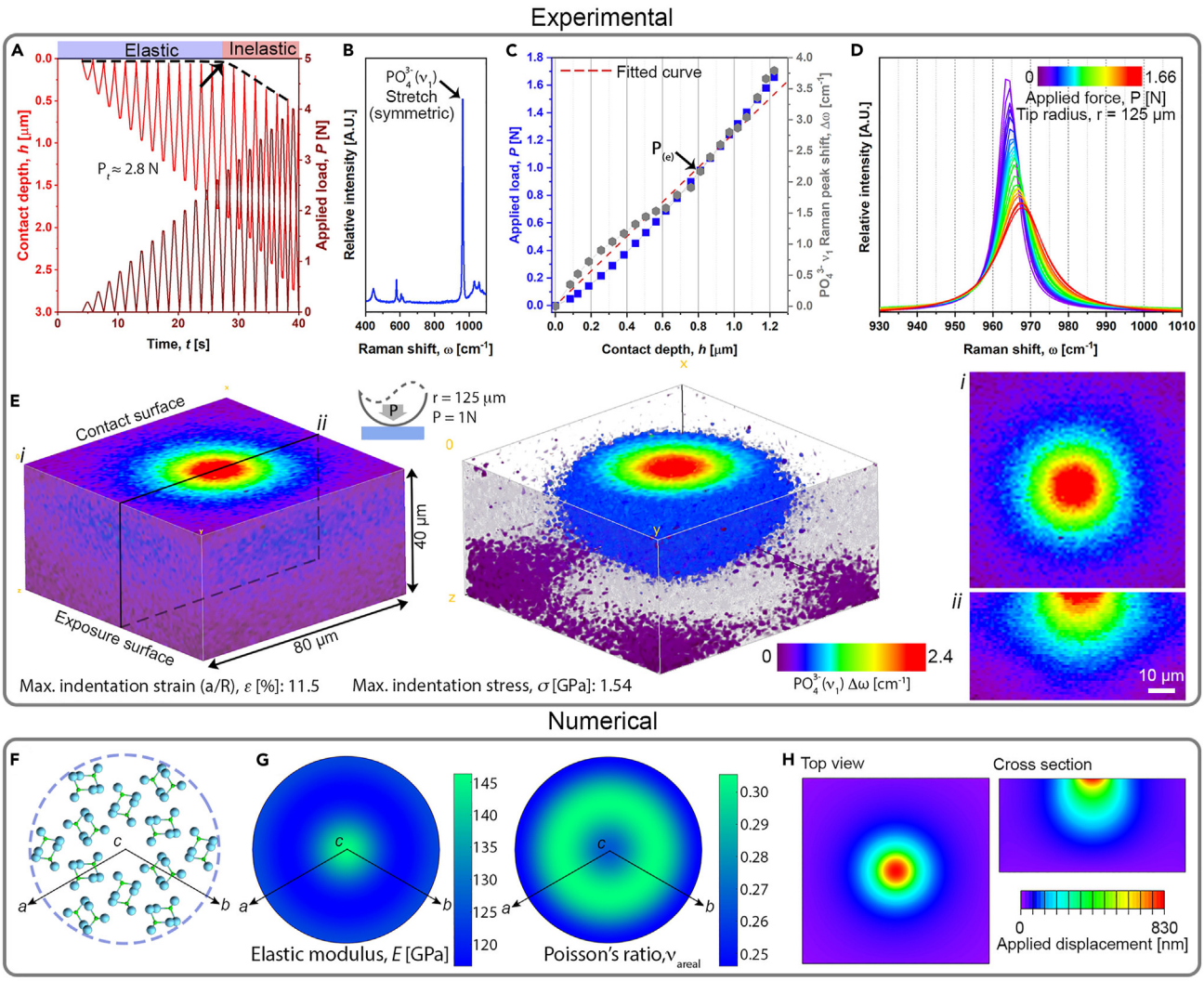

Figure 2. Azimuthal isotropy of EDFs in a geological FAP crystal (001)

(A) Depth-sensing partial loading-unloading nanoindentation using a cono-spherical diamond tip (r = 125 μm) revealing a clear elastic-inelastic transition. The corresponding transition load (p_t) was used to define the elastic loading range to investigate the EDFs.

(B) The most intense peak corresponding to the symmetric stretching mode (ν_1) of the PO_4^{3-} group was used for filtering induced peak shifts and studying the development of EDFs.

(C and D) Correlations between the (C) applied load/displacement and the ν_1 peak position change induced in elastic regimes and (D) associated Raman peaks shifts and broadenings (a transition from the purple color denotes the unloaded state to the red color associated with a maximum load of 1.67 N).

(E) 3D map covering a volume of 80 × 80 × 40 μm^3 with a spatial resolution of 1 μm, constructed of induced peak shifts under contact stress of 1.54 GPa (P = 1 N, h = 0.83 μm), revealing azimuthal isotropy in the developed EDF. Note that, for visualization, the extracted map is rotated 180°, while during the measurements, the contact surface faced downward. Cross-sectional planes (i and ii) present the imaging and virtual sections across and along the loading directions, respectively.

(F and G) Illustrative atomic model of FAP along its 001 direction, modeled using CrystalMaker (F), and corresponding calculated elastic modulus (E) and Poisson's ratio (ν_{31}) plots (G) using AnisoVis,[34] presenting the azimuthal uniformity of elastic contacts in the (001) plane of the geological FAP crystal.

(H) Distribution of contact elastic deformation simulated using similar loading conditions using the finite element method for a loaded geological FAP (001), presenting the azimuthal isotropy in induced EDF.

Despite the anisotropy of elastic characteristics of FAP crystals,[35] the peak position maps revealed azimuthal isotropy in the induced EDF. This azimuthal symmetry is attributed to the loading direction of the FAP sample along its hexagonal symmetry axis[36] (*c* axis). We further investigate the material root of the visualized azimuthal

isotropy using numerical approaches and by first plotting the elastic modulus (E) and Poisson's ratio (ν_{31}) of FAP along its *c* axis (Figure 2F). Figure 2G shows the correlative elastic modulus and Poisson's ratio maps, which are numerically calculated using AnisoVis[34] by implementing the elastic constants of FAP.[35] We then used the elastic constants to simulate the development of elastic strain (principal strain) fields using the finite-element method (Figure 2H) for an identical penetration depth (r = 125 μm, h = 830 nm). Together, numerical approaches presented conformity with the revealed EDF using 3D-RISM (Figures 2E, i and ii; 2G; and 2H).

Azimuthal anisotropy of EDFs in calcite

We next used 3D-RISM to assess the EDFs in geological calcite known for brittleness mainly attributed to the low twinning and cleavage energies of calcite.[37] Geological calcite's elastic-inelastic transition formed at applied loads of $P_t \approx 0.15$ N (Figure 3A), about 18-fold faster than the transition load of geological FAP ($P_t \approx 2.8$ N). Therefore, the EDF mapping on the calcite sample needed to be acquired with minute applied loads requiring high load stability during the long-term 3D scans. Unlike the apparent peak shifts in the FAP sample (Figures 2C and 2D), deformation-induced ν_1 peak shifts in the calcite sample were subtle (<1 cm^{-1}) and formed a sharp and localized gradient in the induced peak shifts. This makes peak shift-deformation coefficient measurements highly susceptible to reading-position errors due to the minuteness of positions with maximum strain/peak shifts and their abrupt movement during stepwise loading. Thus, the peak shift-contact depth correlations (Figure 3C) were performed using 2D depth profiling beneath the contact point, and the maximum peak shift was selected as the peak shift value (Figure S4). On the other hand, collecting such subtle changes in spectra requires the stability of the applied loads, as included in our designed criteria, that can hold the applied loads constant for long-term 3D mapping for up to days (Figure S5).

In stark contrast with the formed azimuthally isotropic EDF developed in geological FAP (001), the strain fields in geological calcite revealed an equilateral trigonal deformation field (Figures 3D and 3E) perpendicular to the loading direction, suggesting a direct interplay between the induced deformations and trigonal crystal system of calcite. One of the key advantages of 3D-RISM is that it can be used *in operando*, so EDFs can be scanned during their development; therefore, we used this option to elaborate on the evolution of the EDF in the calcite sample. We therefore designed an experiment in which the induced Raman shifts were mapped under a stepwise loading cycle, providing fully elastic (P = 84 mN), elastic-inelastic (P = 147 mN), and residual (P = 0) deformations (Figure 3F). The applied loads were selected according to the partial loading-unloading experiment (Figure 3A), and a lateral mapping resolution of 500 nm was selected to accurately visualize the evolving deformation field with high spatial resolution. Remarkably, we found that, by increasing the load toward the elastic-inelastic transition, and while the EDF developed along the vertices, evident by the size increment of the trigonal deformation field, the induced EDF relaxed at the sides (Figures 3E and 3F). This relaxation was evident by subtle recovery of the induced peak shifts, denoting the formation of the tensile strain fields at the edges (Figure 3F, black arrows). This visualization was supported by mapping the unloaded contact zone, revealing residual tension- and compression-induced deformations formed with ~60° shifts around the trigonal symmetry axis of the crystal (Figure 3E, step 3). Our *in operando* measurements demonstrated that increasing the induced isotropic contact stresses and further development of azimuthally anisotropic compression-induced deformations beyond the contact circle (Figure 3F) promote the formation of the tension-induced

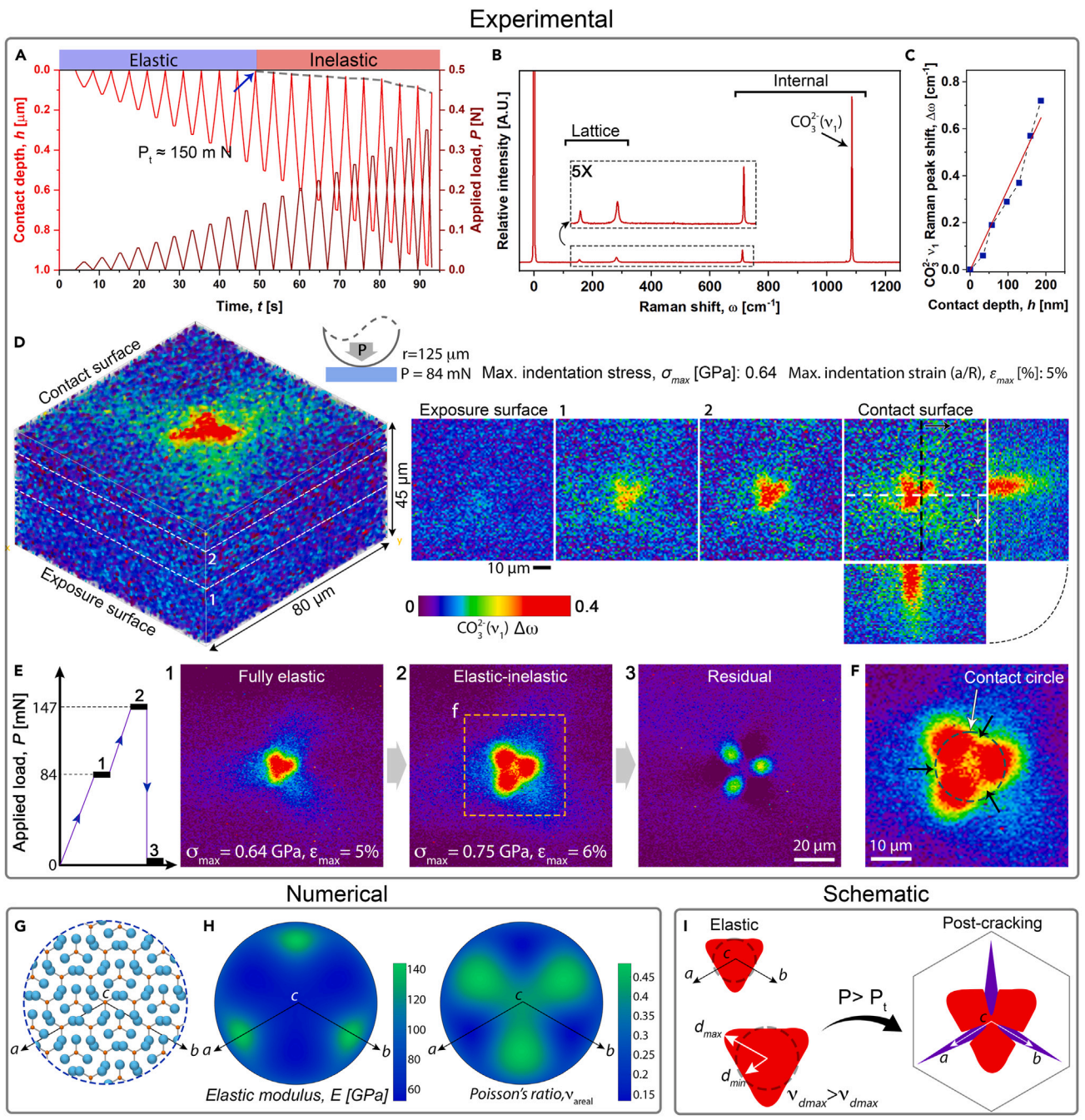

Figure 3. Evolution of azimuthally anisotropic EDFs in calcite (001)

(A) A depth-sensing partial loading-unloading nanoindentation using a diamond cono-spherical tip (r = 125 μm) was used to define the elastic-inelastic transition load (P_t) and select the applied loads required for the formation of different deformation regimes.

(B) The most intense peak corresponding to the symmetric stretching mode (ν_1) of the CO_3^{2-} group was selected for visualizing the induced strains in the 001 plane of the calcite.

(C) Correlative contact depth-peak position shift, calculated and extracted from 2D depth profiles beneath the contact point (Figure S4), allowing an accurate maximum peak shift reading at applied load/displacement.

(D) 3D map and correlated 2D sections of induced elastic deformations under an indentation contact stress of 0.64 GPa (P = 84 mN, h = 0.17 μm, r = 125 μm, map size = 80 × 80 × 45 μm^3, spatial resolution of 1 μm), revealing a triangular strain field beneath Hertzian contact.

(E) *In operando* deformation images acquired at different loading steps, illustrating the evolution of the EDFs at the contact surface during (1) fully elastic (P = 84 mN), (2) elastic-inelastic (P = 147 mN), and (3) residual (P = 0) deformations. Images share the same color scale with the 3D map in (D) and were acquired using a lateral resolution of 500 nm.

Figure 3. *Continued*

(F) The anisotropic advances of the compression strains along the EDF vertices emanate the formation of tension-induced deformations at the edges (black arrows). This causes the relaxation of the induced strains, denoted by a subtle decrement of the Raman peak shifts. The further development of the tension-induced deformations at the higher applied stresses initiates the formation of radial-median microcracks.

(G and H) Illustrative atomic model of calcite along its 001 direction (G) and corresponding calculated elastic modulus (E) and Poisson's ratio (ν_{31}) plots (H) using AnisoVis,[34] presenting the azimuthal uniformity of elastic contacts in the (001) plane of the calcite crystal.

(I) Schematic presenting the development of EDF along the vertices and relaxation of the compression-induced strains at the sides. The direction of the expanding compression strains defines the direction of the radial-median cracks (in blue).

deformations. This eventually regulates the position of the radial-median cracks[1] forming at the higher applied loads.

The direction of the expanding EDFs can be explained by the azimuthal anisotropy of elastic behavior in calcite, evident by elastic modulus (E) and Poisson's ratio (ν_{31}) maps (Figures 2G and 2H), which were numerically calculated using AnisoVis[34] and by implementing the elastic constants of calcite.[38] Together, our *in operando* maps suggest that the azimuthal anisotropy in the development of the compression-induced elastic strains (areas with higher peak shifts), which matches the crystallographic directions with higher Poisson's ratio, define the direction of the radial-median cracks that develop later under higher contact forces (Figure 3I).

Development of EDFs in translucent calcitic prisms of *P. nobilis*

To demonstrate the potential of 3D-RISM for studying EDFs in complex crystals, we used the method to investigate the development of EDFs in a biological ceramic and uncover how the induced EDFs and their development regulate the formation of mechanical damage (inelastic deformations). We chose the calcitic prismatic seashell of *P. nobilis*, where the prisms are elongated along the *c* axis,[23] providing an identical crystallographic direction to our studied geological sample. *P. nobilis* shells contain intercrystalline organic envelopes and intracrystalline organic residues,[23,39] representing an architectured and heterogeneous ceramic. The light transparency of the prismatic shells[40] allowed us to use slices with thicknesses of up to 400 μm supported by a 1-mm quartz backplate for the mapping of the EDFs (Figure 4A). The calcitic prism size ranges from 30–100 μm in diameter (Figures 4B and S6), so targeting the central region of a prism required a precise positioning, which was possible thanks to the 2D translational positioning stage and adjustment screws (Figure 1D). The central region was selected to visualize the development of EDF within a prism and further development to the neighboring prisms (Figure 4B). Depth-sensing partial loading-unloading nanoindentations on *P. nobilis* showed a $P_t \approx 1$ N (Figure S7), revealing an approximately 7-fold increment in transition load compared to the geological counterpart. This can be attributed to the presence of organic residues, which accommodate higher elastic strains and postpone mechanical damage. A contact load of 255 mN, ensuring the elastic response of the sample (Figure S7), was selected for indenting one prism and mapping the induced EDF. We then mapped a volume of 100 × 100 × 50 μm^3 covering the neighbor prisms. This allowed us to investigate the development of induced EDFs to the neighboring prisms separated from each other by a thin (~1 μm at the sides and ~3 μm at the corners) organic shield (Figure S6).

By filtering the ν_1 vibrational band of the CO_3^{2-} group, we first plotted the peak area (Figure 4A), which provides a microarchitectural map of the sample in regard to the position of the calcitic prisms and organic interfaces. This formed a geometrical reference for studying the induced inter- and intra-prismatic strains. Figure 4C presents the organization of organic shields (dark regions) and calcitic prisms (bright regions). We then plotted the peak shifts (Figure 4D) from the same collected map to

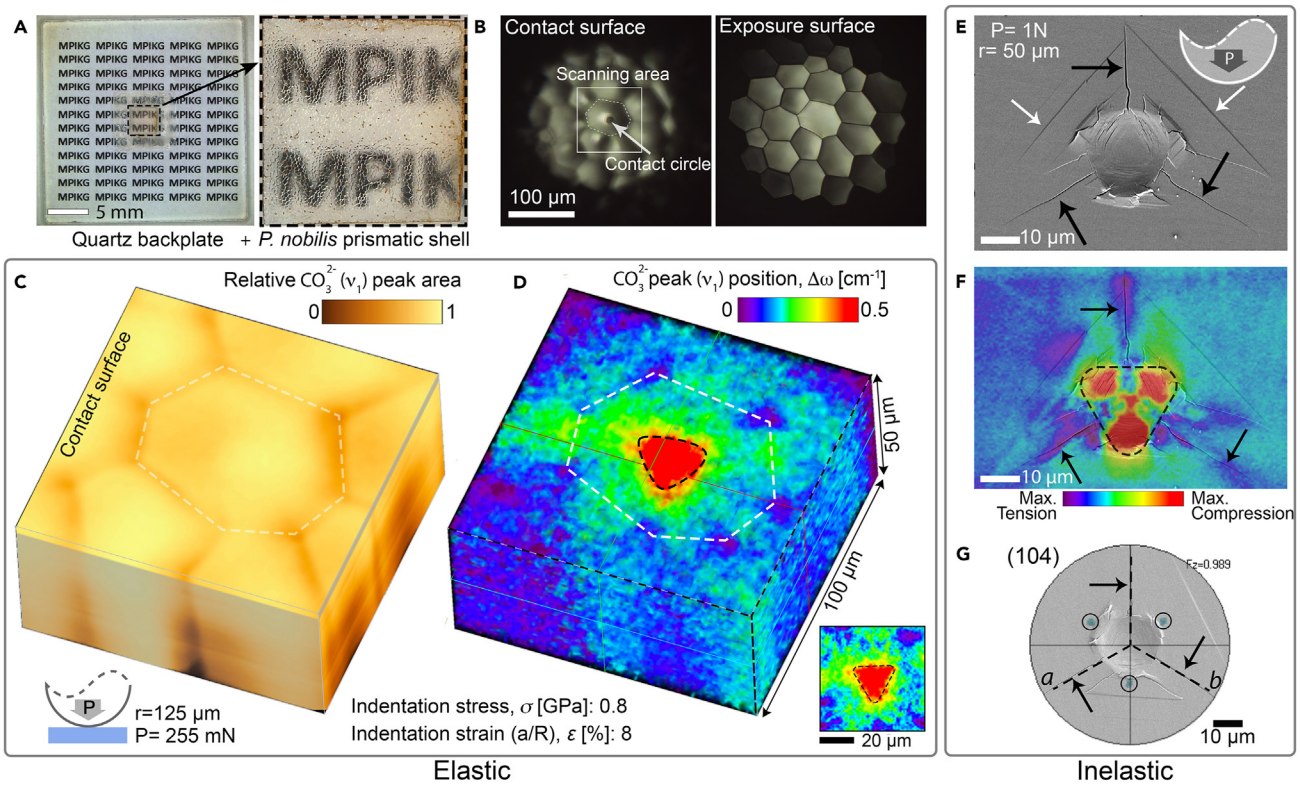

Figure 4. 3D-RISM enables correlative architectural and EDF mapping in translucent biological ceramics

(A) *P. nobilis* prismatic shell slice (t = 240 µm) supported by a quartz backplate was used for EDF mapping. While the presence of a backplate avoids bending deformations, the shell thickness ensures the formation of induced contact deformation away from the shell-backplate interface.

(B) Optical micrographs from the contact surface and exposure surface of the shells.

(C and D) Large 3D mapping, covering a volume of 100 × 100 × 50 μm^3 with a spatial resolution of 1 µm, was used to reveal both inter- and intra-prismatic induced strains.

(C) 3D Raman map of the CO_3^{2-} ν_1 peak area, revealing the arrangement of calcitic prisms (bright regions) and organic shields (dark regions).

(D) EDF map reconstructed based on Raman peak shift of the CO_3^{2-} ν_1 peak in a *P. nobilis* prismatic shell slice (t = 240 µm) under a contact load of P = 255 mN (tip radius, r = 125 µm), revealing the induced EDF within the central prism, marked with dashed lines, and its expansion to the surrounding prisms. The inset in the bottom right corner shows the trigonal EDF formed within the central prism.

(E) Electron micrograph of a residual impression formed at a high contact stress of 1.2 GPa, showing the formation of the microcracks (black arrows) and twinning deformations (white arrows).

(F) Peak shift Raman map (CO_3^{2-} ν_1) showing the 3-sided floral pattern of compression-induced residual deformation, separated by tension-induced microcracks (black arrows).

(G) Post-indentation EBSD pole figure (see the 104 reflection dots, green spots marked with the black circles for better visualization), superimposed on the SEM image of the indented prim with an identical direction, presenting the correlation of the calcite crystallographic geometry, denoted by (104) planes, with the preferred development of the mechanical damage (E).

visualize the developed EDF and correlate it with the architectural organization of prisms (Figures 4B and 4C). Note that the extracted map only represents the deformations in the calcitic prisms, and obviously, the development of mechanical deformations in the organic shields could not be investigated using the selected ν_1 band of the CO_3^{2-} group. In contrast with the geological calcite (Figure 3), the presence of heterogeneities in the calcitic prismatic shell of *P. nobilis* dictated the development of a complex EDF. However, in conformity with the EDFs in the geological calcite (001), the areas with higher peak shifts (peak shift range of ~0.35 cm^{-1} to 0.5 cm^{-1}) revealed a trigonal geometry (Figure 4D, inset). Despite the presence of a continuous organic shield around the prisms (Figure S6) and applying a localized load to the central prisms, there was an apparent expansion of induced deformations from the central prism to the neighboring prisms (Figure 4D, green zones;

peak shift range of ~0.2–0.25 cm^{-1}). This demonstrated that, despite the shielding of the individual prisms by organic envelopes, even under elastic deformations, the organization of neighbor prisms effectively contributes to the mechanical behavior of the individual calcitic prisms.

To unravel the interplay between the development of trigonal EDF and the formation of the inelastic deformations, we first induced localized damage by applying a high contact stress of ~1.2 GPa (P = 1 N, r = 50 μm) and then observed it using field emission scanning electron microscopy (FESEM) and scanning probe microscopy (SPM). Post-indentation micrographs (Figures 4E and S8) revealed a series of trigonal radial-median microcracks and twinning deformations, including those with trigonal organization beneath the contact area (Figures S8B and S8C). We then studied the distribution of the residual strains at the contact zone by mapping the Raman peak shifts on the surface of the residual impression. By filtering the ν_1 vibrational band of the CO_3^{2-} group, we found a 3-sided floral pattern of compression-induced residual strains (Figure 4F), in which compressed sites (positive Raman shift, red color code) were separated by tension-induced microcracks, denoted by negative Raman shifts (purple color code).

We next performed a correlative electron backscatter diffraction (EBSD) study on the indented prisms with residual impressions (Figure 4E) to obtain (104) pole figures representing the orientation of the trigonal symmetry of calcite crystal and correlate the direction of the induced deformations with crystallographic planes of the calcitic prisms. The EBSD pole figures (n = 10) collected from individual indented prisms revealed a clear agreement between the orientation of the mechanical damage and the trigonal arrangement of the calcite (Figure 4G). This confirmed our earlier observation that the preferred development of compressive strain along the facets of the calcite (direction with the highest Poisson's ratio) causes the formation of the tension-induced strain fields along the a and b principal axes of the crystal (Figures 3F–3I). So, the further development of tension-induced strains promotes the formation of the microcracks (Figures 4E, 4F, and S8). Together, the comparison between the revealed EDFs and associated induced microcracking at the higher contact stresses indicate a geometrical correlation between the azimuthal development of EDF and the crystallographic orientation of the calcitic samples.

The interplay of EDF geometry and penetration-induced plasticity

We next used the 3D mapping capability of 3D-RISM to unravel the interplay of subsurface plastic deformations, formed at higher applied stresses, with the geometry of the induced elastic deformations. Accordingly, we first extracted the high-strain deformation fields by plotting the 2D maps for a broader Raman peak shift range of 0–0.8 cm^{-1} and reconstructing the volumetric map of the induced EDF filtered for the upper range of strains (~$0.4 < \Delta\omega < 0.8$ cm^{-1}). This provided an explicit view of the high-strain fields beneath the indenter (Figure 5A), allowing us to picture the geometry of areas exposed to higher induced strains. Remarkably, and in contrast with EDFs introduced in classical Hertzian contact mechanics, the reconstructed 3D map of the induced EDF revealed an unusual trigonal pyramidal geometry with its preferred extension along the c axis of the crystal (Figure 5B). We accordingly hypothesized whether the revealed pyramidal deformation has any correlations with the mechanical damage (deformation in inelastic regimes). Therefore, we first formed a residual indentation impression by applying a contact load of 250 mN using a cono-spherical tip (r = 50 μm). The induced inelastic deformation using the selected combination of low load and tip size allowed us to form a localized deformation beneath the contact area while preventing severe failure

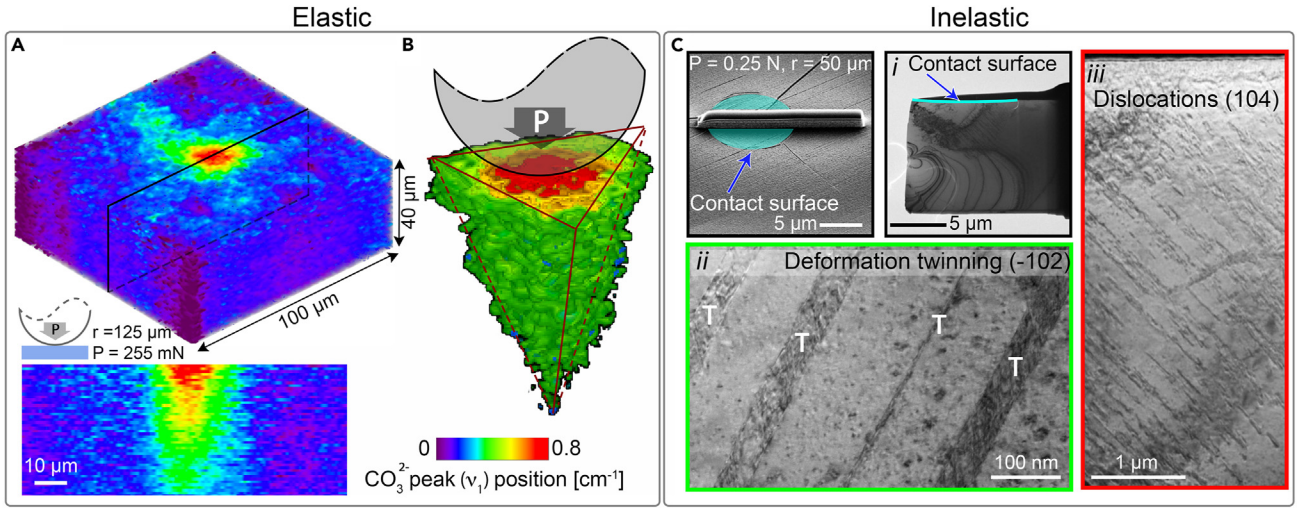

Figure 5. Trigonal pyramidal EDF in calcitic prism of *P. nobilis* shell

(A) 3D EDF map and the virtual depth section of the EDF filtered for the induced peak shift in CO_3^{2-} ν_1 vibrational band, illustrating the formation of a pyramidal elastic field beneath the contact zone (P = 255 mN).

(B) Reconstructed 3D EDF map from the areas with higher peak shifts (0.4–0.8 cm^{-1}), revealing a triangular pyramid geometry, an unusual and distinct EDF from those introduced in classical Hertzian contact mechanics,[29] such as those in Figure 2E.

(C) SEM and TEM micrographs revealing the induced plastic deformations at the high contact stresses. TEM imaging (ii and iii) was done on a FIB-lamella (i) cut from a residual impression of an indented site (area in cyan). TEM micrographs demonstrate that the areas under higher contact stresses (regions in red) result in dislocation deformations (iii), and areas with lower contact strains (regions in green) host the twinning-induced deformations (ii). The direction of the deformation twinning planes (−102) well matches the incline angle of the revealed pyramidal EDF, suggesting the contribution of the crystallographic plane to the elastic response of the calcitic prisms prior to the twinning-induced plasticity.

(Figure 5C). This allowed preparations of transmission electron microscopy (TEM) samples, which covered an area extending from beneath the contact areas to pristine regions (Figure 5C, *i*).

We investigated the sub-surface plastic deformation by applying bright-field diffraction contrast TEM. TEM samples were prepared by the so-called focused ion beam (FIB) technique, which allows slicing thin sections of well-defined orientation. In the present case, thin lamellae (thickness < 100 nm) were cut perpendicular to one edge of the formed trigonal deformations beneath the contact area (Figures 5C and S9). Our TEM observations revealed that the areas with lower contact strains (regions in green) host the twinning-induced deformations (Figure 5C, *ii*) present in deformation-induced twinning along the (−102) planes. In contrast, the areas under higher contact stresses (regions in red) result in dislocation deformations (Figure 5C, *iii*) on (104) planes. Comparing the inclination angle of the pyramidal EDF and the crystallographic angle of the (−102) plane suggests a contribution of the crystallographic plane to the elastic response of the calcitic prisms prior to the twinning-induced plasticity. To the best of our knowledge, such a contribution of the (−102) plane to the mechanical response of biological calcitic systems has not been reported.[41,42]

Conclusions

Despite the advances in the mechanical characterization of biological ceramics and their geological counterparts,[6,15,27,41,43–45] 3D and *in operando* imaging of EDFs in materials research remains a challenging task, preventing a full assessment of complex material deformation mechanisms. This has been mainly attributed to the limitations and complexities in methodological approaches allowing the formation, measurement, and visualization of the EDFs with suitable spatial resolution required

for studying localized deformations. To address the current limitations, we devised 3D-RISM, an approach based on confocal Raman microspectroscopy combined with a customized inverted miniaturized nanoindenter integrated into a translational stage equipped with a large optical window. Together, they allow the mapping of induced localized deformations beneath the contact loads, *in operando*, with submicron spatial resolution, and in 3D.

We applied our method to study the evolution of indentation EDFs in two crystal systems of FAP and calcite and revealed how crystallographic structure influences the development of EDFs. Our method substantially revealed a complex relationship between the crystallographic organization of a biological ceramic with an externally induced EDF *in operando* and in 3D, providing new insights into the role of materials architecture in the distribution of elastic-inelastic deformations. Besides, our work emphasizes the importance of spherical indentation to avoid the effect of azimuthal directionality in the mechanical response of crystalline ceramics.[46,47]

We demonstrated that 3D-RISM introduces an efficient approach capable of (1) direct visualization of the elastic deformations without simplifying assumptions about surface roughness and Poisson's ratio; (2) imaging elastic deformations perpendicular to the loading directions, which allows mapping of azimuthal anisotropy of Poisson's ratio; (3) *in operando* mapping of deformation under varying applied loads, so contact stresses can be increased stepwise, and the temporal evolution of elastic and inelastic deformation can be accurately imaged; (4) simultaneous 3D mapping of deformation and chemical/structural features (sensitivity to both organic and inorganic components), making our method an apt technique for studying elastic deformation in biological materials; and (5) unraveling the structural roots of mechanical damage. Therefore, we anticipate that 3D-RISM can be an important step toward a quantitative understanding of the evolution of complex elastic deformations, which has been poorly understood so far. Moreover, 3D-RISM opens new avenues for unraveling the interplay between elastic anisotropy, materials' microarchitecture, and mechanical performance in hybrid materials and microdevices. Our method can transform our considerations of the significance of EDF geometries, their azimuthal anisotropy, and their impact on the formation of mechanical damage.

EXPERIMENTAL PROCEDURES

Resource availability

Lead contact

Requests for further information and resources should be directed to and will be fulfilled by the lead contact, Shahrouz Amini (shahrouz.amini@mpikg.mpg.de).

Materials availability

This study did not generate new unique materials.

Data and code availability

All data generated during the study are available from the lead contact upon reasonable request. This study did not generate a code.

Sample preparation

Geological apatite was bought from a local mineral shop and was sectioned perpendicularly to the *c* axis of the sample. The *c* axis of the sample was selected according to the hexagonal geometry of the crystal and was confirmed with polarized Raman spectroscopy and X-ray diffraction. Geological calcite slices (001) were purchased from a commercial source. Single crystal-like biological samples of *P. nobilis* were

received from Y. Dauphin (Centre national de la recherche scientifique, Sorbonne Université, Muséum National d'Histoire Naturelle), whose support is acknowledged by the authors. The sample was sectioned perpendicular to the growth direction of the shell (*c* axis of calcite). Samples were mechanically polished with P1200/4000-grade silicon carbide paper and then 1-μm diamond paste. After polishing, the diamond particles and polishing debris were removed from the sample in an ultra-bath of 50% ethanol for 5 min.

Microstructural imaging and characterization

Microstructural imaging was performed using FESEM (JEOL 7500F, Japan) at a low 5-kV accelerating voltage. The surface of polished samples was coated with Pt to avoid charging effects during imaging.

Inverse nanoindentation

Inverse nanoindentation studies were performed using a piezo actuator with a step size of 5 nm (Physical Instrument, USA) equipped with a miniature load cell (Futek, USA) and a customized 125-μm cono-spherical diamond tip. A digital motion controller (Physical Instrument, Germany) and MicroMove software (Physical Instrument, Germany) were used to operate the piezo actuator. An in-line miniature load cell (Futek) and Sensit software (Futek) were used for recording the loads during the measurements. A metallic 2D stage composed of a lockable ring sandwiched between two frames was used for mounting and positioning the sample (Figure 1). The samples were mounted on a fused quartz backplate (t = 1 mm) and then fixed on the sample holder ring with a wide optical window of 11 mm. The position of the sample was adjusted and fixed using four fine screws. Together, this combination allows the locking of the movable ring prior to loading the sample. The metallic frame, stage, and optical window were fabricated in our in-house machine shop at the Max Planck Institute of Colloids and Interfaces (Potsdam, Germany).

Depth-sensing nanoindentation

Nanoindentation was conducted using a triboindenter (TI-950 nanomechanical tester, Hysitron, USA). To calculate the elastic-inelastic transition load of the samples, a 3D omni-probe high load transducer (Bruker, Hysitron) with a 125-μm cono-spherical fluid cell tip (Bruker, Hysitron) was used. To induce permanent mechanical deformations on the *P. nobilis* sample (Figures 4D, 4E, 4G, and 5C), a 3D omni-probe equipped with a 50-μm cono-spherical fluid cell tip was used to facilitate the formation of the residual impressions.

Friction coefficient measurement

Friction coefficient measurement on the FAP slice was performed using a triboindenter (TI-950 nanomechanical tester, Hysitron) equipped with a cono-spherical diamond tip (r = 125 μm) using a contact load of 1 mN. A scratch track of 100 μm was used for the measurements.

SPM

SPM was performed using a triboindenter (TI-950 nanomechanical tester, Hysitron) equipped with a 2D transducer. The SPM images in Figures S1 and S8 were obtained using Berkovich and cube corner indenters, respectively. A set load of 2 μN was used for the mappings.

Raman spectroscopy

High-resolution Raman maps and point measurements were obtained using a confocal Raman microscope (alpha300R, WITec, Ulm, Germany) together with a 532-nm laser

source with a laser intensity of 40 mW (for geological samples)/30–35 mW (for biological samples) and a ×20 objective lens with an NA of 0.35 (Carl Zeiss, Germany). A spectrometer (UHTS 600, WITec) equipped with two gratings of 2,400 gr/mm (for *P. nobilis* shell and geological calcite) and 1,800 gr/mm (for geological FAP) was used for the Raman mappings. The acquisition parameters of each Raman map are reported in the figure legends.

Data analysis

Collected Raman maps were processed for the removal of cosmic rays and background prior to peak position analysis using Project Five (v.5.2, WITec). Next, the selected peaks of 963 cm^{-1} and 1,086 cm^{-1}, attributed to PO_4^{3-} and CO_3^{2-} groups in FAP and calcite, respectively, were fitted using a Lorentzian fitting function using Project Five (v.5.2). The color codes were assigned using the "Color Scale" tab of the software for individual 2D maps. The initial range of 2D Raman map scale bars was automatically selected based on the lowest and highest Raman shifts. So, to generate correlative maps for 3D reconstructions, the range of the assigned color codes was manually defined by selecting the minimum and maximum peak shift values within the entire individual 2D scans. Plotting was done using OriginPro software. The 3D reconstruction of the Raman maps was done using the Volume Viewer plugin of the ImageJ software. The segmented pyramidal EDF (Figure 5B) was performed using Amira (v.6.5, FEI).

Numerical mapping of elastic modulus (E) and Poisson's ratio (ν)

Considering the anisotropy of the selected material models, the elastic constant of the FAP and calcite crystals was adapted from Sha et al.[35] and Chen et al.,[38] respectively, and then the elastic modulus (E) and Poisson's ratio (ν_{31}) maps for the required directions were plotted using AnisoVis[34] in MATLAB.

Finite element modeling

3D nonlinear finite element modeling was employed to estimate the contact dynamics between the spherical diamond tip and the FAP sample. Surface-to-surface contact between the two bodies was modeled with the specification of a hard normal contact and a penalty tangential contact with a coefficient of friction of 0.23. The FAP crystal was modeled as fully anisotropic following the stiffness matrix values in Sha et al.[35] The coefficient of friction was measured in a tribological experiment using a diamond tip and the FAP sample (see friction coefficient measurement). The diamond tip was modeled as isotropic material with a Young's modulus of 1,000 GPa and Poisson's ratio of 0.2. The model was simulated as displacement controlled along the crystal *c* axis and with a dynamic implicit solver using the commercial modeling software Abaqus (Dassault Systemes, Simulia, RI, USA).

FIB lamella sample preparation

TEM lamellae were prepared using an FEI/Thermo Fisher Scientific Versa 3D dual-beam scanning electron microscope/FIB with a Ga ion source. Lamellae were prepared from the primary sample and thinned with ions at an accelerating voltage of 30 kV. They were then finally polished on both sides in the FIB with 5-kV and 2-kV Ga ions at an angle of 4° and 6°, respectively.

TEM

For the TEM investigations, a JEM-ARM200F (JEOL) was used, operated at an acceleration voltage of 200 kV. This high-resolution electron microscope (double corrected) was equipped with a goniometer, allowing the samples to be tilted up to ±30°. Thereby, the crystalline FIB lamellae could be investigated in different appropriate crystallographic orientations, such as [100], [010], and [110]. Thereby,

the formed/generated planar defects and dislocations could be analyzed. For imaging and analysis of these defects, the following TEM techniques were applied: (1) conventional bright-field diffraction contrast, (2) high-resolution lattice plane imaging, and (3) electron diffraction. The images were recorded by a 4k-OneView camera and analyzed and processed by the Digital Micrograph software (Gatan, USA). For the simulation of the crystal structure of the calcite lattice and its related electron diffraction pattern, the CrystalMaker/SingleCrystal software was used (CrystalMaker Software).

EBSD

To understand the possible correlations between the induced microcracks and crystallographic orientation (rotation around the *c* axis) of the *P. nobilis* prisms, EBSD measurements were performed on indented samples (n = 10). First, polished prisms were indented using a cono-spherical tip (r = 50 μm) and an applied load of 700 mN to induce microcracking. Then, EBSD measurements were carried out on the indented prisms using a Hitachi SU5000 field emission SEM equipped with an EBSD detector (Oxford Instruments). To prevent charging, sample surfaces were coated with 4–6 nm of carbon. During EBSD measurements, the SEM was operated at 20 kV. EBSD scans were performed with a step size ranging from 200 to 400 nm. For obtaining color-coded crystal orientation maps and corresponding pole figures, EBSD measurements were evaluated with the Oxford Instruments AZTEC and CHANNEL 5 HKL software.

SUPPLEMENTAL INFORMATION

Supplemental information can be found online at https://doi.org/10.1016/j.matt.2024.06.006.

ACKNOWLEDGMENTS

The authors acknowledge Yannicke Dauphine for providing the *P. nobilis* shell sample, Frank Heyroth for preparing the FIB-lamella preparation used for the TEM studies, and R.J. Hickey (Pennsylvania State University) and C. Micheletti (Max Planck Institute of Colloids and Interfaces, Department of Biomaterials) for the helpful discussion and careful review of the manuscript. The project was funded by the Max Planck Society.

AUTHOR CONTRIBUTIONS

The idea of the method and design of the experiments were developed by S.A. and P.F. The miniaturized indenter was designed and fabricated by S.A. The *in operando* measurements were conducted and analyzed by S.A. and T.Z. S.A., P.F., and T.Z. discussed the results of the *in operando* measurements. H.R. conducted the finite element modeling analysis. E.G. conducted and analyzed the EBSD measurements. P.W. conducted the TEM study and analyzed the crystallographic data. S.A. wrote the manuscript with input from all co-authors.

DECLARATION OF INTERESTS

S.A. and P.F. are the inventors of the methodology patented by the Max-Planck-Gesellschaft zur Förderung der Wissenschaften e.V. (patent nos. EP20220172138 and WO2023213647).

Received: March 1, 2024
Revised: May 2, 2024
Accepted: June 4, 2024
Published: July 3, 2024

REFERENCES

1. Lawn, B. (1993). Fracture of Brittle Solids, 2nd Edition (Cambridge University Press). https://doi.org/10.1017/CBO9780511623127.
2. Amini, S., Tadayon, M., Idapalapati, S., and Miserez, A. (2015). The role of quasi-plasticity in the extreme contact damage tolerance of the stomatopod dactyl club. Nat. Mater. *14*, 943–950. https://doi.org/10.1038/nmat4309.
3. Cook, R.F. (2019). Fracture sequences during elastic–plastic indentation of brittle materials. J. Mater. Res. *34*, 1633–1644. https://doi.org/10.1557/jmr.2019.112.
4. Bernier, J.V., Suter, R.M., Rollett, A.D., and Almer, J.D. (2020). High-Energy X-Ray Diffraction Microscopy in Materials Science. Annu. Rev. Mater. Res. *50*, 395–436. https://doi.org/10.1146/annurev-matsci-070616-124125.
5. Ecker, W., Keckes, J., Krobath, M., Zalesak, J., Daniel, R., Rosenthal, M., and Todt, J. (2020). Nanoscale evolution of stress concentrations and crack morphology in multilayered CrN coating during indentation: Experiment and simulation. Mater. Des. *188*, 108478. https://doi.org/10.1016/j.matdes.2020.108478.
6. Gim, J., Schnitzer, N., Otter, L.M., Cui, Y., Motreuil, S., Marin, F., Wolf, S.E., Jacob, D.E., Misra, A., and Hovden, R. (2019). Nanoscale deformation mechanics reveal resilience in nacre of Pinna nobilis shell. Nat. Commun. *10*, 4822. https://doi.org/10.1038/s41467-019-12743-z.
7. Legros, M. (2014). In situ mechanical TEM: Seeing and measuring under stress with electrons. Compt. Rendus Phys. *15*, 224–240. https://doi.org/10.1016/j.crhy.2014.02.002.
8. Haciane, R., Bilek, A., Larbi, S., and Said, D. (2015). Photoelastic and Numerical Analysis of a Sphere/Plan Contact Problem. Procedia Eng. *114*, 277–283. https://doi.org/10.1016/j.proeng.2015.08.069.
9. Tuschel, D. (2019). Stress, strain, and Raman spectroscopy. Spectroscopy *34*, 10–21.
10. Wermelinger, T., Borgia, C., Solenthaler, C., and Spolenak, R. (2007). 3-D Raman spectroscopy measurements of the symmetry of residual stress fields in plastically deformed sapphire crystals. Acta Mater. *55*, 4657–4665. https://doi.org/10.1016/j.actamat.2007.04.036.
11. Wermelinger, T., and Spolenak, R. (2018). Stress Analysis by Means of Raman Microscopy. In Confocal Raman Microscopy, J. Toporski, T. Dieing, and O. Hollricher, eds. (Springer International Publishing), pp. 509–529. https://doi.org/10.1007/978-3-319-75380-5_21.
12. He, L.-H., Carter, E.A., and Swain, M.V. (2007). Characterization of nanoindentation-induced residual stresses in human enamel by Raman microspectroscopy. Anal. Bioanal. Chem. *389*, 1185–1192. https://doi.org/10.1007/s00216-007-1520-8.
13. Korsunsky, A.M. (2017). Chapter 8 - Residual Stress "Measurement". In A Teaching Essay on Residual Stresses and Eigenstrains, A.M. Korsunsky, ed. (Butterworth-Heinemann), pp. 93–107. https://doi.org/10.1016/B978-0-12-810990-8.00008-2.
14. Dhiman, A., Lewis, N.S., Dillard, T., Sudarshan, M., and Tomar, V. (2021). Advancements in mechanical Raman spectroscopy for applications in energetic materials. Energetic Materials Frontiers *2*, 193–200. https://doi.org/10.1016/j.enmf.2021.09.001.
15. Loh, H.-C., Divoux, T., Gludovatz, B., Gilbert, P.U.P.A., Ritchie, R.O., Ulm, F.-J., and Masic, A. (2020). Nacre toughening due to cooperative plastic deformation of stacks of co-oriented aragonite platelets. Commun. Mater. *1*, 77. https://doi.org/10.1038/s43246-020-00078-y.
16. Pezzotti, G. (2005). Raman piezo-spectroscopic analysis of natural and synthetic biomaterials. Anal. Bioanal. Chem. *381*, 577–590. https://doi.org/10.1007/s00216-004-2780-1.
17. Delbé, K., De Sousa, C., Grizet, F., Paris, J.-Y., and Yahiaoui, M. (2022). Determination of the Pressure Dependence of Raman Mode for an Alumina–Glass Pair in Hertzian Contact. Materials *15*, 8645.
18. Wasmer, K., Wermelinger, T., Bidiville, A., Spolenak, R., and Michler, J. (2008). In situ compression tests on micron-sized silicon pillars by Raman microscopy—Stress measurements and deformation analysis. J. Mater. Res. *23*, 3040–3047. https://doi.org/10.1557/JMR.2008.0363.
19. Amini, S., and Fratzl, P. (2023). Strain Measurement Apparatus and Method For Measuring Mechanical Strain. Germany patent EP 22172138, patent application 22172138.4. filed April 26, 2023, and published September 11, 2023.
20. Gerbig, Y.B., Michaels, C.A., Forster, A.M., Hettenhouser, J.W., Byrd, W.E., Morris, D.J., and Cook, R.F. (2012). Indentation device for in situ Raman spectroscopic and optical studies. Rev. Sci. Instrum. *83*, 125106. https://doi.org/10.1063/1.4769995.
21. Gayle, A.J., Friedman, L.H., Beams, R., Bush, B.G., Gerbig, Y.B., Michaels, C.A., Vaudin, M.D., and Cook, R.F. (2017). Two-dimensional strain-mapping by electron backscatter diffraction and confocal Raman spectroscopy. J. Appl. Phys. *122*, 205101. https://doi.org/10.1063/1.5001270.
22. Myers, G.A., Hazra, S.S., de Boer, M.P., Michaels, C.A., Stranick, S.J., Koseski, R.P., Cook, R.F., and DelRio, F.W. (2014). Stress mapping of micromachined polycrystalline silicon devices via confocal Raman microscopy. Appl. Phys. Lett. *104*, 191908. https://doi.org/10.1063/1.4878616.
23. Dauphin, Y., Zolotoyabko, E., Berner, A., Lakin, E., Rollion-Bard, C., Cuif, J.P., and Fratzl, P. (2019). Breaking the long-standing morphological paradigm: Individual prisms in the pearl oyster shell grow perpendicular to the c-axis of calcite. J. Struct. Biol. *205*, 121–132. https://doi.org/10.1016/j.jsb.2019.01.004.
24. Li, H., Xin, H.L., Kunitake, M.E., Keene, E.C., Muller, D.A., and Estroff, L.A. (2011). Calcite Prisms from Mollusk Shells (*Atrina Rigida*): Swiss-cheese-like Organic–Inorganic Single-crystal Composites. Adv. Funct. Mater. *21*, 2028–2034. https://doi.org/10.1002/adfm.201002709.
25. Zolotoyabko, E. (2017). Anisotropic Lattice Distortions in Biogenic Minerals Originated from Strong Atomic Interactions at Organic/Inorganic Interfaces. Adv. Mater. Interfac. *4*, 1600189. https://doi.org/10.1002/admi.201600189.
26. Seknazi, E., and Pokroy, B. (2018). Residual Strain and Stress in Biocrystals. Adv. Mater. *30*, 1707263. https://doi.org/10.1002/adma.201707263.
27. Amini, S., Razi, H., Seidel, R., Werner, D., White, W.T., Weaver, J.C., Dean, M.N., and Fratzl, P. (2020). Shape-preserving erosion controlled by the graded microarchitecture of shark tooth enameloid. Nat. Commun. *11*, 5971. https://doi.org/10.1038/s41467-020-19739-0.
28. Hecht, E. (2012). Optics (Pearson Education India).
29. Lawn, B.R. (1998). Indentation of Ceramics with Spheres: A Century after Hertz. J. Am. Ceram. Soc. *81*, 1977–1994. https://doi.org/10.1111/j.1151-2916.1998.tb02580.x.
30. Pezzotti, G. (1999). In situ study of fracture mechanisms in advanced ceramics using fluorescence and Raman microprobe spectroscopy. J. Raman Spectrosc. *30*, 867–875. https://doi.org/10.1002/(SICI)1097-4555(199910)30:10<867::AID-JRS466>3.0.CO;2-0.
31. Pezzotti, G. (2013). Raman spectroscopy of piezoelectrics. J. Appl. Phys. *113*, 211301. https://doi.org/10.1063/1.4803740.
32. Masic, A., and Weaver, J.C. (2015). Large area sub-micron chemical imaging of magnesium in sea urchin teeth. J. Struct. Biol. *189*, 269–275. https://doi.org/10.1016/j.jsb.2014.12.005.
33. Field, J.S., and Swain, M.V. (1993). A simple predictive model for spherical indentation. J. Mater. Res. *8*, 297–306. https://doi.org/10.1557/JMR.1993.0297.
34. Healy, D., Timms, N.E., and Pearce, M.A. (2020). The variation and visualisation of elastic anisotropy in rock-forming minerals. Solid Earth *11*, 259–286. https://doi.org/10.5194/se-11-259-2020.
35. Sha, M.C., Li, Z., and Bradt, R.C. (1994). Single-crystal elastic constants of fluorapatite, Ca5F(PO4)3. J. Appl. Phys. *75*, 7784–7787. https://doi.org/10.1063/1.357030.
36. Shrikanth, S., Knowles, K.M., Neelakantan, S., and Prasad, R. (2020). Planes of isotropic Poisson's ratio in anisotropic crystalline solids. Int. J. Solid Struct. *191–192*, 628–645. https://doi.org/10.1016/j.ijsolstr.2019.10.014.
37. Bruno, M., Massaro, F.R., Rubbo, M., Prencipe, M., and Aquilano, D. (2010). (10.4), (01.8), (01.2), and (00.1) Twin Laws of Calcite ($CaCO_3$): Equilibrium Geometry of the Twin Boundary Interfaces and Twinning Energy. Cryst. Growth Des. *10*, 3102–3109. https://doi.org/10.1021/cg100233p.
38. Chen, C.-C., Lin, C.-C., Liu, L.-G., Sinogeikin, S.V., and Bass, J.D. (2001). Elasticity of single-crystal calcite and rhodochrosite by Brillouin spectroscopy. Am. Mineral. *86*, 1525–1529. https://doi.org/10.2138/am-2001-11-1222.

39. Gilow, C., Zolotoyabko, E., Paris, O., Fratzl, P., and Aichmayer, B. (2011). Nanostructure of Biogenic Calcite Crystals: A View by Small-Angle X-Ray Scattering. Cryst. Growth Des. *11*, 2054–2058. https://doi.org/10.1021/cg200136t.

40. Amini, S., Zhu, T., Biswas, A., Charsooghi, M.A., Kim, K., Reber, S., Dauphin, Y., and Fratzl, P. (2023). Calcitic Prisms of The Giant Seashell Pinna Nobilis Form Light Guide Arrays. Adv. Mater. *35*, 2304166. https://doi.org/10.1002/adma.202304166.

41. Deng, Z., Chen, L., and Li, L. (2023). Comparative nanoindentation study of biogenic and geological calcite. J. Mech. Behav. Biomed. Mater. *137*, 105538. https://doi.org/10.1016/j.jmbbm.2022.105538.

42. Castillo Alvarez, C., Grimsich, J.L., Schmidt, C.A., Lisabeth, H., Voigtländer, A., and Gilbert, P.U.P.A. (2023). Calcite Twinning in Mollusk Shells and Carrara Marble. Adv. Funct. Mater. 2304288. https://doi.org/10.1002/adfm.202304288.

43. Lew, A.J., Stifler, C.A., Tits, A., Schmidt, C.A., Scholl, A., Cantamessa, A., Müller, L., Delaunois, Y., Compère, P., Ruffoni, D., et al. (2023). A Molecular-Scale Understanding of Misorientation Toughening in Corals and Seashells. Adv. Mater. *35*, 2300373. https://doi.org/10.1002/adma.202300373.

44. Ihli, J., Clark, J.N., Kanwal, N., Kim, Y.-Y., Holden, M.A., Harder, R.J., Tang, C.C., Ashbrook, S.E., Robinson, I.K., and Meldrum, F.C. (2019). Visualization of the effect of additives on the nanostructures of individual bio-inspired calcite crystals. Chem. Sci. *10*, 1176–1185. https://doi.org/10.1039/C8SC03733G.

45. Marcus, M.A., Amini, S., Stifler, C.A., Sun, C.-Y., Tamura, N., Bechtel, H.A., Parkinson, D.Y., Barnard, H.S., Zhang, X.X.X., Chua, J.Q.I., et al. (2017). Parrotfish Teeth: Stiff Biominerals Whose Microstructure Makes Them Tough and Abrasion-Resistant To Bite Stony Corals. ACS Nano *11*, 11856–11865. https://doi.org/10.1021/acsnano.7b05044.

46. Kunitake, M.E., Mangano, L.M., Peloquin, J.M., Baker, S.P., and Estroff, L.A. (2013). Evaluation of strengthening mechanisms in calcite single crystals from mollusk shells. Acta Biomater. *9*, 5353–5359. https://doi.org/10.1016/j.actbio.2012.09.030.

47. Böhm, C.F., Feldner, P., Merle, B., and Wolf, S.E. (2019). Conical Nanoindentation Allows Azimuthally Independent Hardness Determination in Geological and Biogenic Minerals. Materials *12*, 1630.